

> REPLACE THIS LINE WITH YOUR MANUSCRIPT ID NUMBER (DOUBLE-CLICK HERE TO EDIT) <

# Simplified Coherent Photonics-aided D-band Fiber-THz Integrated System with Adaptive Kramers-Kronig Scheme and Probabilistic Shaping

Yaxuan Li, Boyu Dong, Penghao Luo, An Yan, Sizhe Xing, Yinjun Liu, Ziwei Li, Chao Shen, Jianyang Shi, Nan Chi and Junwen Zhang

**Abstract**—Simplified coherent detection technology is a promising solution for saving receiver costs in ultra-high data rate photonic-aided terahertz communication systems. One of the key issues in the simplified system when using envelope detector (ED) is that the generation of signal-to-signal beating interferences (SSBI) reduces the signal-to-noise ratio (SNR). Kramers-Kronig (KK) algorithm could effectively eliminate SSBI. In this study, we demonstrated the feasibility of adaptive KK (AKK) in a simplified coherent photonics-aided terahertz system in the D-band. Nonlinearity and inter symbol interference (ISI) are two major challenges that limit the capacity and rate of terahertz systems. The advantage of adaptive KK lies not only in effectively eliminating nonlinearity in the system, but also in considering the impact of ISI and incorporating equalizers into the AKK scheme. Simulation and experimental results show that AKK has improvement in terms of driving voltage range, received optical power, and carrier signal power ratio (CSPR) compared to traditional KK methods. Furthermore, based on proposed AKK scheme, a line rate of over 80 Gbps and a net rate of over 60 Gbps are realized through 10-km standard single-mode fiber (SSMF) and 0.5-m wireless distance with the probabilistic shaping (PS) technology in the 137-GHz fiber-THz integrated communication system.

**Index Terms**—Kramers-Kronig receiver, nonlinearity and inter symbol interference, photonics-aided terahertz communication system, simplified coherent detection

This work was supported in part by the National Key Research and Development Program of China under Grant 2022YFB2903600, in part by the National Natural Science Foundation of China under Grants 62235005, 62171137, 61925104, and 62071444, in part by the Natural Science Foundation of Shanghai under Grant 21ZR1408700, and in part by the Major Key Project PCL. (Corresponding author: Junwen Zhang and Jianyang Shi.)

Yaxuan Li, Boyu Dong, Penghao Luo, An Yan, Sizhe Xing, Yinjun Liu are with the Key Laboratory for Information Science of Electromagnetic Waves (MoE), Department of Communication Science and Engineering, Fudan University, Shanghai 200433, China (e-mail: 23110720079@m.fudan.edu.cn; bydong21@m.fudan.edu.cn; phluo22@m.fudan.edu.cn; ayan22@m.fudan.edu.cn; szxing21@m.fudan.edu.cn; 23110720080@m.fudan.edu.cn).

Ziwei Li, Chao Shen, Jianyang Shi, Nan Chi and Junwen Zhang are with the Key Laboratory for Information Science of Electromagnetic Waves (MoE), Department of Communication Science and Engineering, Fudan University, Shanghai Engineering Research Center of Low-Earth-Orbit Satellite Communication and Applications, Shanghai Collaborative Innovation Center of Low-Earth-Orbit Satellite Communication Technology, Fudan University, Shanghai 200433, China, and also with the Peng Cheng Laboratory, Shenzhen 518055, China (e-mail: lizw@fudan.edu.cn; chaoshen@fudan.edu.cn; jy\_shi@fudan.edu.cn; nanchi@fudan.edu.cn; junwenzhang@fudan.edu.cn).

## I. INTRODUCTION

As the sixth-generation (6G) mobile communication technology with lower latency, higher capacity, and greater spectrum sharing approaches us, terahertz (THz) technology, as one of the key technologies in 6G communication, has also attracted widespread attention [1], [2]. THz technology has broad development prospects in various fields such as radar systems, absorbing materials and applications, biomedical research, spectral imaging technology, detection and sensing, etc. Due to its abundant absolute bandwidth resources, THz has broad application potential in the field of communication. THz band is adjacent to microwave on the left and infrared light on the right in the spectrum. THz communication combines the dual advantages of microwave communication and optical communication, with characteristics such as high carrier frequency and wide bandwidth. A wide spectrum range is a good information carrier, which could greatly increase the communication capacity and solve the current problems of spectrum scarcity, capacity limitation, difficulty in fiber optic access, and high cost in the field of wireless systems [3], [4].

In recent years, with the advancement of THz sources, detectors, optical components and other related technologies, photonics-aided THz communication architectures have gradually matured [5], [6], [7], [8]. Photonics-aided THz technology uses Uni-Travelling-Carrier photodiodes (UTC-PD) or PIN photodiodes (PIN-PD) as optical mixers, effectively converting optical signals into electrical signals. Then, the antenna structure around the optical mixer converts the photocurrent into THz waves. Photonics-aided THz also allows for easy integration of these wireless links into fiber optic infrastructure, making it highly suitable for radio access network (RAN) scenarios, as illustrated in Fig. 1.

The spectral efficiency of coherent modulation is generally higher than intensity-only modulation. Therefore, complex signals with quadrature amplitude modulation (QAM) formats are commonly used in optical fiber and wireless communication systems to increase capacity [9], [10], [11]. However, traditional complex signal reception and demodulation require coherent detection. Conventional full-coherent receivers based on dual-polarization intradyne detection cost is too high for fiber-THz integrated system. In past research, many simplified coherent receivers have been

> REPLACE THIS LINE WITH YOUR MANUSCRIPT ID NUMBER (DOUBLE-CLICK HERE TO EDIT) <

proposed for coherent translation [12], [13], [14]. Simplified coherent receiver design based on single-polarization heterodyne detection and Alamouti coding has recently emerged only requiring a 3-dB coupler and a balanced photodiode (BPD). Moreover, researchers have tried to replace the BPD with a single-ended photodiode (SPD).

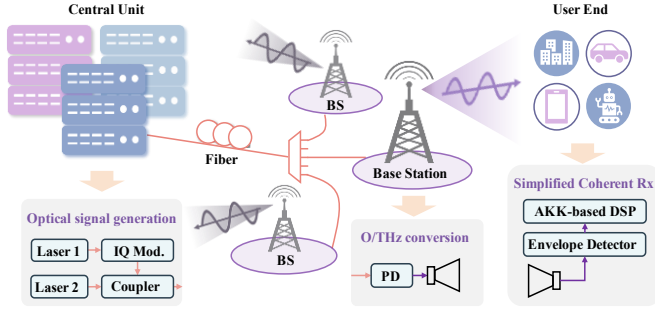


**Fig. 1.** Simplified coherent D-band fiber-THz integrated communication system.

Kramers-Kronig (KK) algorithm is a method for eliminating SSBI in simplified coherent reception, which was proposed in 2016 [15]. Inspired by such scheme in optical communication system, there are also many demonstrations of simplified coherent THz system with KK scheme [16], [17]. T Harter et al. proposed the generalized Kramers-Kronig (GKK) receiver in 2020 [16]. GKK scheme accounts for the real characteristics of the Schottky-barrier diode (SBD) and leads to a substantial performance improvement compared with conventional square-root KK processing or with heterodyne reception without guard band. Recently, a spectrally efficient polarization division multiplexed (PDM) twin single-sideband (twin-SSB) transmission scheme for direct-detection THz communication systems used KK algorithm effectively eliminate the signal-to-signal beating interferences and contributes to better polarization de-multiplexing [17]. In our previous work [18], we demonstrated a simplified coherent W-band fiber-MMW integrated system with an envelope-detector at user-end for complex-signal detection, enabled by the adaptive KK algorithm. An adaptive KK (AKK) method was utilized to mitigate the impact of SSBI by considering the nonlinearity of the entire MMW system response.

In addition to the receiving technologies mentioned above, probabilistic shaping (PS) is an optimization technique for encoding and modulation and recently been applied to THz communication systems to improve the overall capacity [19], [20], [21], [22]. PS technology has been proven to fully improve the spectral efficiency of the system and dynamically adjust its capacity [23]. The average power of the signal after PS is lower than the original signal, which is beneficial for the power limitation caused by nonlinear problems in THz communication systems. Under the same signal-to-noise ratio (SNR), the Euclidean distance between constellation points after PS is improved, resulting in improved fault tolerance. The use of PS could help to approach channel capacity and achieve higher transmission rates and reliability after channels with nonlinearity (NL) and inter symbol interference (ISI)

caused by THz frequency-selective fading and uneven device amplitude response.

In this paper, we optimize the AKK scheme by further considering the impact of the location and strength of system nonlinearity on performance meanwhile adding processing of ISI caused by unsatisfactory system transmission characteristics based on our previous work [18]. We also extend the simplified coherent detections scheme to a higher frequency band, namely, D-band in the fiber-THz integrated system from W-band in [18], and adopt PS technology to adapt to system channel conditions for higher data rate realization. In terms of nonlinearity, we perform the amplitude-to-amplitude (AM-AM) measurement between the absolute value of transmitted signal and received signal, and then use the least squares (LS) algorithm for fitting curve applied to replace the square root operation in traditional KK algorithm. Unlike [18] only treated the system nonlinearity as a result, we provide detailed theoretical analyses and simulation verification about how the AKK performance affected whether nonlinearity occurs before or after the envelope detector (ED) at the receiver. At the same time, in the field of ISI processing, a least mean squares (LMS) equalizer is added to the AKK scheme. which was not considered in reference [18]. Herein, we explain the detailed principle of AKK scheme and then numerical simulation results for the strength of system nonlinearity which occurs before/after ED and different ISI intensities are provided. In a simulation system with nonlinearity and ISI, AKK performs better than GKK. Finally, we conduct an experimental demonstration in a simplified coherent photonics-aided D-band fiber-THz integrated system with AKK scheme based on PS-QAM modulations. The experimental results also confirm that AKK has better performances in terms of nonlinearity and ISI impairments. Based on the AKK scheme, a line rate of over 80 Gbps and a net rate of over 60 Gbps are realized through 10-km standard single-mode fiber (SSMF) and 0.5-m wireless distance in the 137-GHz fiber-THz integrated communication system.

## II. PRINCIPLES

### A. Kramers-Kronig Receiver

In [15], the principle of KK coherent receiver has been explained. Commonly, in the case of a single-sideband signal  $s(t) = s_r(t) + is_i(t)$ , the real part and imaginary part are related through the KK relations:

$$\begin{aligned} s_r(t) &= -p.v. \int_{-\infty}^{\infty} \frac{s_i(t') dt'}{\pi(t-t')}, \\ s_i(t) &= p.v. \int_{-\infty}^{\infty} \frac{s_r(t') dt'}{\pi(t-t')}. \end{aligned} \quad (1)$$

where p.v. stands for principal value. Equation (1) could be proved based on Fourier transform and inverse Fourier transform of single-sideband signal. Now define  $1+s(t) = |1+s(t)| \exp[i\phi(t)]$  and take the logarithm of the

> REPLACE THIS LINE WITH YOUR MANUSCRIPT ID NUMBER (DOUBLE-CLICK HERE TO EDIT) <

equation  $S(t) = \log[1 + s(t)] = \log|1 + s(t)| + i\phi(t)$ . The new signal  $S(t)$  has the real part  $\log|1 + s(t)|$  and the imaginary part  $\phi(t)$ . It has been demonstrated  $S(t)$  is also single sideband when  $|s(t)| < 1$ , and hence  $|S(t)|$  and  $\phi(t)$  are also related through KK relations identical to (1), implying the equality

$$\begin{aligned} \phi(t) &= p.v. \int_{-\infty}^{\infty} \frac{\log|1 + s(t')|}{\pi(t-t')} dt' \\ &= p.v. \int_{-\infty}^{\infty} dt' \frac{\log|1 + s(t')|^2}{2\pi(t-t')}. \end{aligned} \quad (2)$$

Consider signal of any amplitude  $E_s(t) = E_0 s(t)$ , where  $E_0$  is a real positive quantity, it could be obtained

$$\phi_E(t) = p.v. \int_{-\infty}^{\infty} dt' \frac{\log[(E_0^2)|1 + s(t')|^2]}{2\pi(t-t')}, \quad (3)$$

where  $(E_0^2)|1 + s(t)|^2 = |E_0 + E_s(t)|^2 = i(t)$  are the received signal produced by devices that meet the square-law response such as PD, ED, or power detector. Therefore, (3) can be used to reconstruct the signal phase as follows:

$$\phi_E(t) = H(\log(\sqrt{i(t)})) \quad (4)$$

where  $H(\cdot)$  represents Hilbert transform.

### B. Generalized Kramers-Kronig Receiver

However, the SBD as a broadband and compact envelope detector in THz communication system features non-quadratic rectification characteristics, thus requiring a generalization of the KK-based signal reconstruction algorithm. GKK scheme was proposed in [16], assuming that the relationship between the amplitude of the THz signal at the SBD receiver input  $|E_0 + E_s(t)|$  and the current at the output  $i(t)$  can be described by a bijective function  $g$

$$i(t) = g(|E_0 + E_s(t)|) \quad (5)$$

The amplitude can then be reconstructed by applying the

inverse function  $g^{-1}(i)$ , and the phase can be found by replacing  $\sqrt{i(t)}$  in (4) with the generalized expression  $g^{-1}(i(t))$ :

$$\phi_E(t) = H(\log(g^{-1}(i(t)))) \quad (6)$$

### C. Adaptive Kramers-Kronig Receiver

The GKK architecture considers the response characteristics of SBD, but it does not analyze other nonlinearities present in the fiber-THz integrated system and the influence of ISI in the KK architecture. However, nonlinearities and ISI are inevitable. Therefore, we further optimize KK and propose an adaptive KK architecture.

Consider a system model as shown in Fig. 2.

The ideal THz signal could be expressed as  $S_1 = [E_0 + E_s(t)] \exp[2\pi j(f_2 - f_1)t]$ , in which  $f_1$  and  $f_2$  are the frequency of signal light and local oscillator light respectively for photonics-aided THz generation, and  $f_2 - f_1$  is the THz carrier frequency generated by photomixing. Affected by the NL before ED  $f_{NL1}(\cdot)$ , the input signal of ED could be expressed as  $S_2 = f_{NL1}(S_1)$ . For the convenience of derivation, we use the simple square term to represent nonlinearity here and parameter  $a_1$  to measure the nonlinear strength.

$$f_{NL1}(x) = x + a_1 x^2 \quad (7)$$

So, the input signal of ED

$$\begin{aligned} S_2 &= [E_0 + E_s(t)] \exp[2\pi j(f_2 - f_1)t] \\ &+ a_1 [E_0 + E_s(t)]^2 \exp[4\pi j(f_2 - f_1)t] \end{aligned} \quad (8)$$

The output signal of ED  $S_3$  could be obtained by the ideal ED square law of signal  $S_2$ , and then through a NL function  $f_{NL2}(x) = x + a_2 x^2$  equivalently.

$$\begin{aligned} |S_2|^2 &= S_2 \cdot S_2^* = |E_0 + E_s(t)|^2 + a_1^2 |E_0 + E_s(t)|^4 \\ &+ a_1 |E_0 + E_s(t)|^2 [E_0 + E_s(t)] \exp[2\pi j(f_2 - f_1)t] \\ &+ a_1 |E_0 + E_s(t)|^2 [E_0 + E_s(t)]^* \exp[2\pi j(f_1 - f_2)t] \end{aligned} \quad (9)$$

Because of the low pass filter in the ED, the last two THz

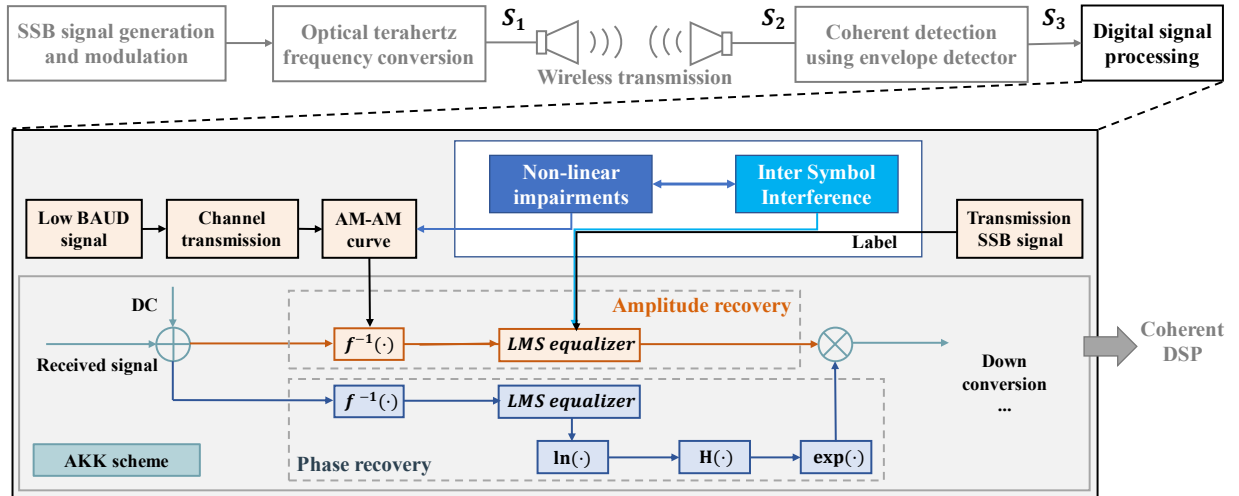


Fig. 2. Simplified coherent THz communication system model and AKK scheme.

> REPLACE THIS LINE WITH YOUR MANUSCRIPT ID NUMBER (DOUBLE-CLICK HERE TO EDIT) <

frequency components of  $|S_2|^2$  cannot output. Therefore, the real signal after ED and amplifier could be expressed as

$$\begin{aligned} S_3 &= f_{NL2}(|E_0 + E_s(t)|^2 + a_1^2 |E_0 + E_s(t)|^4) \\ &= |E_0 + E_s(t)|^2 + a_1^2 |E_0 + E_s(t)|^4 \\ &\quad + a_2(|E_0 + E_s(t)|^2 + a_1^2 |E_0 + E_s(t)|^4)^2 \\ &= |E_0 + E_s(t)|^2 + (a_1^2 + a_2)|E_0 + E_s(t)|^4 \\ &\quad + 2a_1^2 a_2 |E_0 + E_s(t)|^6 + a_1^4 a_2 |E_0 + E_s(t)|^8 \\ &= k_1 |E_0 + E_s(t)|^2 + k_2 |E_0 + E_s(t)|^4 \\ &\quad + k_3 |E_0 + E_s(t)|^6 + k_4 |E_0 + E_s(t)|^8 \\ &= f(|E_0 + E_s(t)|) \end{aligned} \quad (10)$$

where  $f$  is the system NL, and the coefficients of higher-order terms  $k$  in it are nonlinear combination of coefficients  $a_1$  and  $a_2$  in the nonlinear function before and after ED. To eliminate the inaccuracy of nonlinearity in the amplitude and phase recovery of KK architecture, we proposed using polynomial fitting of the system AM-AM curve to obtain system NL function  $f$ . The phase can be reconstructed as follows:

$$\phi_E(t) = H(\log(f^{-1}(S_3))) \quad (11)$$

Next, ISI is considered to exist, performing as time domain response  $h_1$  before ED and  $h_2$  after ED. The received signal is influenced as follows:

$$\begin{aligned} S_3 &= |E_0 + E_s(t)|^2 * h_1(t) * h_2(t) \\ &= |E_0 + E_s(t)|^2 * h(t) \end{aligned} \quad (12)$$

The phase can be reconstructed as  $\phi_E(t) = H(\log(S_3 * h^{-1}(t)))$  after obtaining the inverse of the system response  $h^{-1}(t)$  through an LMS equalizer. It is worth noting that the labels used in the equalizer are the real part of the ideal signal aligned in the frequency domain. In the LMS equalizer, the training sequence length is 4000 with a frame length of 174080. The ratio of training data length to effective data length is approximately 0.0235. In this way, improvements are made in the KK architecture to address NL and ISI in the system. AKK scheme aims to more accurately recover the original complex signal.

#### D. AM-AM curves

In the previous section, we mentioned using AM-AM curves to estimate the NL response of the system. Specifically, the principles are following:

A series of signals are transmitted, and the waveform amplitude could be expressed as  $Tx(n)$ . After transmitting through system channel, the voltage amplitude of the synchronized received intermediate frequency signal  $Rx(n) = f(Tx(n))$ , in which  $f(\cdot)$  means system response.

The system AM-AM response could be obtained by plotting points of transmitted data amplitude against the corresponding received signal amplitude. In order to fit these scattered points into nonlinear AM-AM curve, we used polynomial fitting.

Therefore  $f^{-1}(\cdot)$  could be expressed as a power series with  $M + 1$  initially unknown coefficients  $a_i$ , the transmitted data

$$Tx(n) = f^{-1}(Rx(n)) = \sum_{i=0}^M a_i Rx(n)^i.$$

The coefficients could be obtained from a least-squares fit of the polynomial function with known  $Tx(n)$  and  $Rx(n)$ . The calculated AM-AM curves will replace the square root in the AKK scheme to more accurately reconstruct complex data. In order to reduce the impact of ISI on fitting accuracy, we specifically used sampled data of low baud signal for AM-AM curves fitting.

#### E. Adding pilot in digital signal processing

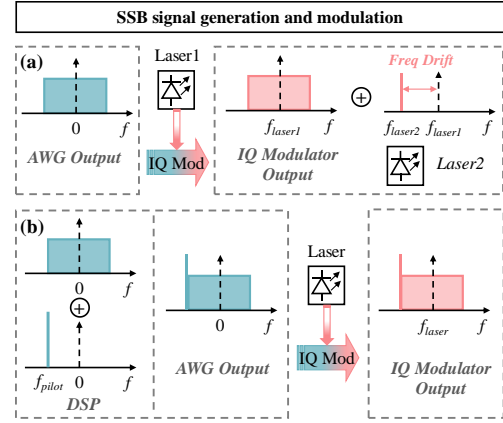


**Fig. 3.** SSB signal generation process with adding pilot in (a) analog domain and (b) digital domain.

Many previous works have added virtual carriers in analog domain in similar SSB systems [16], [17], [24], [25]. We used a method of adding tone in the digital domain, and the specific operation process is shown in Fig. 3(b). After generating the baseband complex signal in digital signal processing (DSP), we would generate a direct-current signal and up-convert it to the bandwidth side of the baseband signal. Finally, add the baseband signal and the generated tone together and send to arbitrary waveform generator (AWG).

The use of adding tone in the digital domain has some advantages over the analog domain. At the transmitting end, it reduces the use of one laser, thereby reducing the complexity and cost of the link. Secondly, the frequency difference between the baseband signal and tone added in the digital domain is fixed and not affected by laser frequency drift. The method we proposed stabilizes the frequency offset of the received intermediate frequency signal, thereby avoiding the frequency offset correction processing of the receiver DSP, increasing system stability and reducing software complexity.

### III. SIMULATION AND RESULTS

Initially, numerical simulations were conducted on a simplified coherent D-band photonics-aided THz communication system to test the performance of the AKK scheme compared to conventional KK, and GKK processing schemes. The impact of different implementation conditions, such as the strength of system nonlinearity which occurs before/after ED, and ISI strengths were investigated in the simulation.



> REPLACE THIS LINE WITH YOUR MANUSCRIPT ID NUMBER (DOUBLE-CLICK HERE TO EDIT) <

### A. Simulation Setup

The simulation was conducted by using commercial optical simulation software VPIphotonics Design Suite™. The simulation setup is shown in the Fig. 4. Baseband data was generated in MATLAB, then the optical communication and photoelectric conversion were simulated in VPI, and finally the THz signal was down converted in MATLAB, passed through NL and ISI block, AKK processing and other DSPs. The up-sampling rate used in simulation all KK cases is 8. The parameters in VPI are summarized in Table I.

TABLE I PARAMETERS OF THE SIMULATION	
Simulation Parameters	Values
Laser linewidth	100 kHz
Laser average power	0 dBm
Laser1 frequency	193.1 THz
Laser2 frequency	193.237 THz
MZM V <sub>pi</sub>	5 V
PIN responsivity	0.7 A/W
PIN thermal noise	10 <sup>-12</sup> A/Hz <sup>1/2</sup>
Sample rate	400 GHz

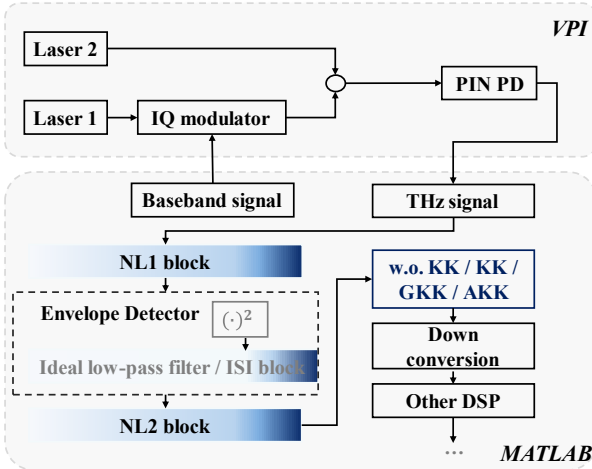


**Fig. 4.** Simulation setup of the simplified coherent D-band photonics-aided THz communication system.

QPSK and 16QAM signals with a bandwidth of 20 GHz were transmitted in the simulation system. The THz carrier frequency was set to 137 GHz, and the received THz signal first passed through module NL1 to simulate nonlinearity occurring during fiber and THz frequency transmission. Then, it passed through ED, which was replaced by a numerical square function and a low-pass filter. Then, it passed through module NL2 to simulate the imperfect response curve of ED, as well as the nonlinearity that may occur in intermediate frequency and baseband. ISI strength could be adjusted by controlling the frequency response of low-pass filter in ED. The ideal low-pass filter refers to the filter that completely attenuates signals above the cutoff frequency and transmits

signals below the cutoff frequency without distortion. Although it does not exist, we use it to simulate system without ISI.

### B. Nonlinearity and Results

AKK's resistance to nonlinearity was first validated. The two nonlinear simulation modules NL1 and NL2 in the simulation system have the function of not adding nonlinearity, adding weak or strong nonlinearity to the signal waveform. The amplitude nonlinearity of fiber terahertz channels was mainly studied. Due to the saturation effects, the amplitude transfer curve exhibits an "S" shape. Specifically, an approximate function could be used to fit the S-shaping nonlinear effect as [26]

$$f_{NL}(x) = \frac{a}{1 + e^{-bx}} + c \quad (13)$$

with  $a$ ,  $b$ , and  $c$  are the fitted parameters. Parameter  $a$  zooms the y-axis, adjusting the output amplitude. Parameter  $b$  scales the x-axis, reflecting the different strength of nonlinearity. Parameter  $c$  is the bias to ensure that the output at point 0 is 0. Three strengths of nonlinearity were set: no NL, weak NL, and strong NL. The three nonlinear model functions are shown in the Fig. 5, and the corresponding parameters  $a$ ,  $b$ , and  $c$  are listed in Table II.

TABLE II PARAMETERS OF THE NL FUNCTIONS			
NL Strength	Simulation Parameters Values		
	a	b	c
Weak NL	2.168	3.21	-1.084
Strong NL	2.008	5.838	-1.004

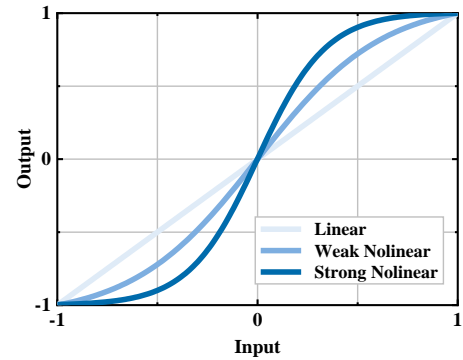


**Fig. 5.** Nonlinearity block functions.

The nonlinearity of the system in the simulation is divided into two parts: before and after ED. This division is consistent with the nonlinear effects of real communication systems. Moreover, in the simulation, the strength of these two parts can be adjusted separately, which cannot be achieved in the experimental system. This makes it easier to verify the superiority of AKK under different nonlinear cases.

> REPLACE THIS LINE WITH YOUR MANUSCRIPT ID NUMBER (DOUBLE-CLICK HERE TO EDIT) <

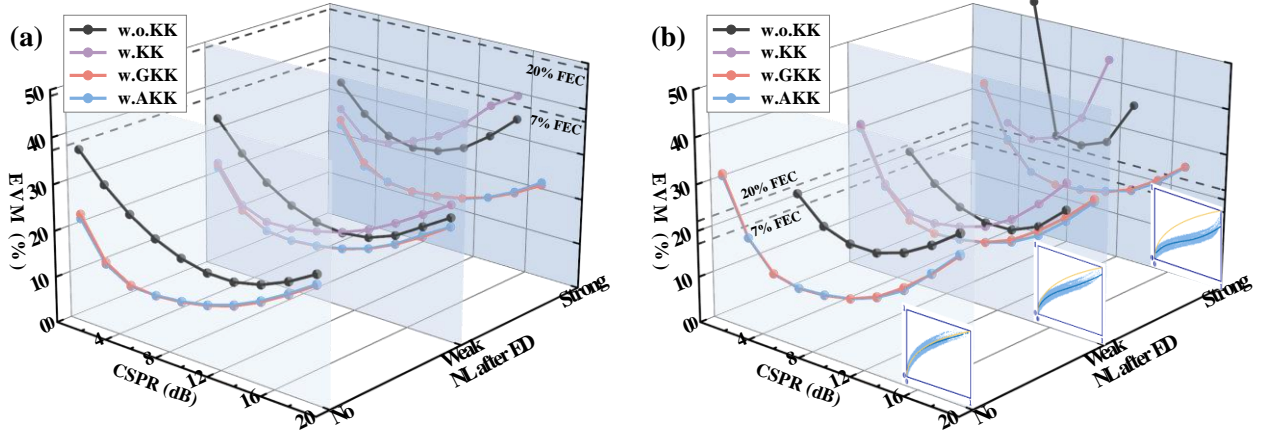


**Fig. 6.** Simulation EVM results for 20-GBd (a) QPSK and (b) 16QAM as functions of CSRR and strength of nonlinearity after ED.

In the simulation comparing the performance among no KK, KK, GKK, and AKK in the presence of nonlinearity, ISI was not artificially introduced for fairness, despite the theoretical equalization effect of AKK on ISI. Therefore, an ideal low-pass filter was used in the ED to transform the signal to the frequency domain through Fast Fourier Transform (FFT), set the frequency components outside the cut-off frequency (40 GHz) to zero, and then recover the time-domain signal via Inverse Fast Fourier Transform (IFFT), thus eliminating the differential impact of ISI under different nonlinear conditions.

Firstly, it is assumed that the system only has NL2, which means that ED does not satisfy square law detection. Because ISI has hardly been introduced, the effect of AKK should be similar to that of GKK. Because the high SNR of system supports QPSK error free transmission, we use the error vector magnitude (EVM) instead of BER to measure the performance for consistency.

EVM is a measure for the effective distance of the received complex symbols  $E_r$  from their ideal positions  $E_t$  in the constellation [27]. Specifically, it relates the root-mean-square value  $\sigma_{err}$  of the error vector amplitude  $|E_r - E_t|$  to the root-mean-square value of the  $N$  ideal constellation points:

$$EVM = \frac{\sigma_{err}}{|E_t|}, |E_t|^2 = \frac{1}{N} \sum_{n=1}^N |E_{t,n}|^2, \sigma_{err}^2 = \frac{1}{N} \sum_{n=1}^N |E_{r,n} - E_{t,n}|^2 \quad (14)$$

With this calculation method, EVM embraces all (linear and nonlinear) impairments. It should be noted that when further calculating BER in practical applications, the influence of the “fly away” points affected by the KK operation should be considered [28]. Fig. 6 shows EVMs of QPSK signal and 16QAM signal as a function of carrier signal power rate (CSRR) at different strength of NL2. The curves of GKK and AKK performance almost overlap. It is worth mentioning that the GKK curve depicted in the figure is an ideal case, using a known ED response curve, while the curve used by AKK is entirely from LS polynomial fitting. Therefore, it can be seen there are sporadic points where fitting errors may cause slight and acceptable differences between GKK and AKK. On the other hand, the results also confirm that the accuracy and robustness of LS algorithm for curve fitting. The illustration

depicts AM-AM curves of the system with no NL, weak NL, and strong NL from left to right.

However, in actual systems, nonlinearity not only exists in the ED and beyond, but also commonly occurs before the ED, such as when high peak-to-peak voltage ( $V_{pp}$ ) output from the arbitrary waveform generator (AWG) and large received optical power (ROP) of PD are used in the system. Therefore, verification of nonlinearity before the ED was conducted. This part of the simulation includes 9 cases, which are combinations of different nonlinear strengths of NL1 and NL2,

**TABLE III**

NONLINEAR CONDITIONS CORRESPONDING TO EACH CASE		
Case	NL before ED	NL after ED
1	No	No
2	No	Weak
3	No	Strong
4	Weak	No
5	Weak	Weak
6	Weak	Strong
7	Strong	No
8	Strong	Weak
9	Strong	Strong

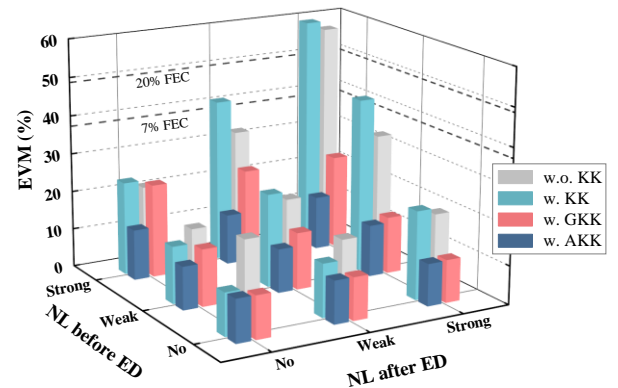


**Fig. 7.** Simulation EVM for 20-GBd QPSK in different nonlinearity cases 1-9 with 7-dB CSRR.

> REPLACE THIS LINE WITH YOUR MANUSCRIPT ID NUMBER (DOUBLE-CLICK HERE TO EDIT) <

respectively. The nonlinear conditions corresponding to each case are provided in Table III.

From Fig. 6, the optimal CSRR for using GKK and AKK scheme in our simulation system is 7 dB. The Fig. 7 and Fig. 8 present a performance comparison of QPSK and 16QAM signals under different cases, with CSRR value of 7 dB. It can be observed that when nonlinearity exists before the ED, the performance of AKK is superior to that of GKK, especially in cases 7-9 where the nonlinearity before the ED is relatively strong. This demonstrates the adaptability of AKK, which is effective against various types of nonlinearities. Compared to GKK, AKK utilizes an adjustable system AM-AM curve to minimize the impact of nonlinearity on signal transmission.

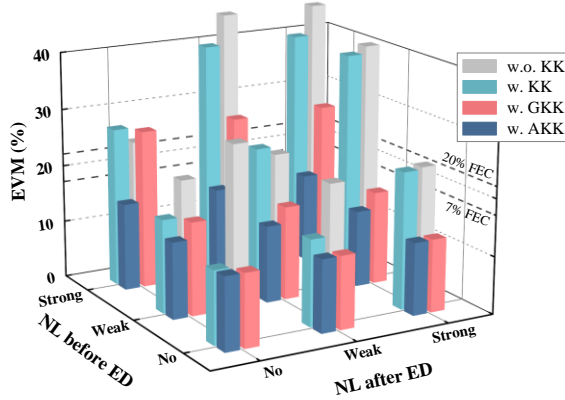


**Fig. 8.** Simulation EVM for 20-GBd 16QAM in different nonlinearity cases 1-9 with 7-dB CSRR.

### C. ISI and Results

The strength of ISI in the simulation system could be adjusted by modifying the passband of the non-ideal low-pass filter in the ED. In this part, the ideal low-pass filter is replaced with a Butterworth low-pass filter, which is set to have an attenuation of less than 3 dB within the passband and more than 10 dB within the stopband. The passband frequency and stopband frequency are set as  $W_p$  and  $W_s$ , respectively, satisfying a certain formula:

$$\begin{aligned} W_p &= B \cdot \text{ratio} \\ W_s &= 2B \cdot \text{ratio} \end{aligned} \quad (15)$$

where  $B$  is the bandwidth of the signal. The *ratio*, varying between 0.4 and 1, is used to adjust the ISI strength. A lower ratio corresponds to stronger ISI, equivalent to applying a fading (as shown in the Fig. 9(b)) after squaring the received THz signal. The filter passband bandwidths corresponding to ratios of 0.4, 0.5, 0.6, 0.7, 0.8, 0.9, and 1.0 are 8, 10, 12, 14, 16, 18, and 20 GHz, respectively, and the corresponding stopband bandwidths are 16, 20, 24, 28, 32, 36, and 40 GHz.

Fig. 9(a) demonstrates the change in EVM for a 16QAM signal as ISI varies. The solid lines represent the performance in case 1, and the dashed lines show the results in case 2. When CSRR is fixed at 7dB, the LMS equalizer in AKK provides compensation for ISI and AKK outperforms GKK and KK. The improvement is less significant when ISI is weak but becomes more pronounced as ISI increases. However, when the ISI intensity is too strong, the performance gain

brought by the LMS equalizer will be limited. Since GKK ideally compensates for the nonlinearity in case 2, the improvement from the red dashed line (GKK) to the blue dashed line (AKK) represents the additional gain achieved by AKK's ISI equalization in case 2. Therefore, our simulation concludes that AKK performs better than GKK in a system with both nonlinearity and ISI.

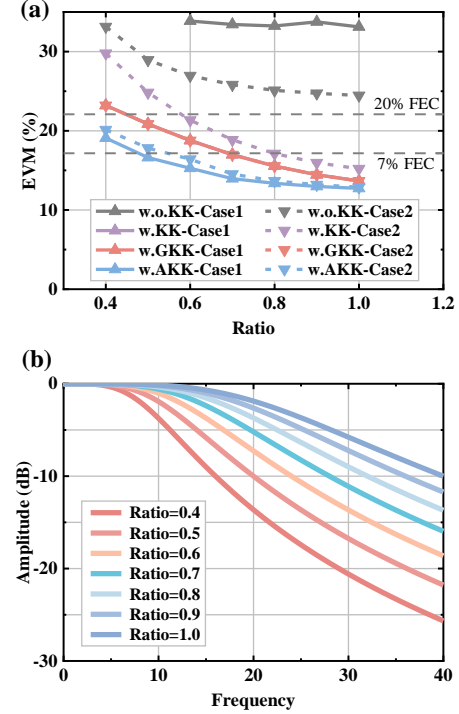


**Fig. 9.** Simulation EVM for 20-GBd 16QAM as a function of ISI strength ratio in (a) nonlinearity cases 1&2, (b) ISI fading in simulation system.

## IV. EXPERIMENTAL DEMONSTRATION AND RESULTS

In the simulation section, we presented the performance of AKK under different nonlinearity and ISI intensities. After verification in the simulation system, we further conducted experimental demonstration to verify whether AKK scheme could work in real systems that are much more complex and unknown than the simulation nonlinearity and ISI conditions.

### A. Experimental Setup

Fig. 10 shows the experimental setup and the DSP details for a simplified coherent photonics-aided D-band fiber-THz integrated system with AKK scheme based on PS-QAM modulations. At the transmitter, the bit data was mapped into PS-QAM constellations with the support of the constant composition distribution matching method (CCDM) and after being up-sampled, it passed through a root-raised cosine (RRC) pulse shaping filter. As mentioned earlier, we generated a pilot single tone signal offline through DSP at the edge of the signal spectrum. The baseband signal with added tone was converted from digital domain to analog domain using 120GSa AWG, and modulated onto an optical carrier with a frequency of

> REPLACE THIS LINE WITH YOUR MANUSCRIPT ID NUMBER (DOUBLE-CLICK HERE TO EDIT) <

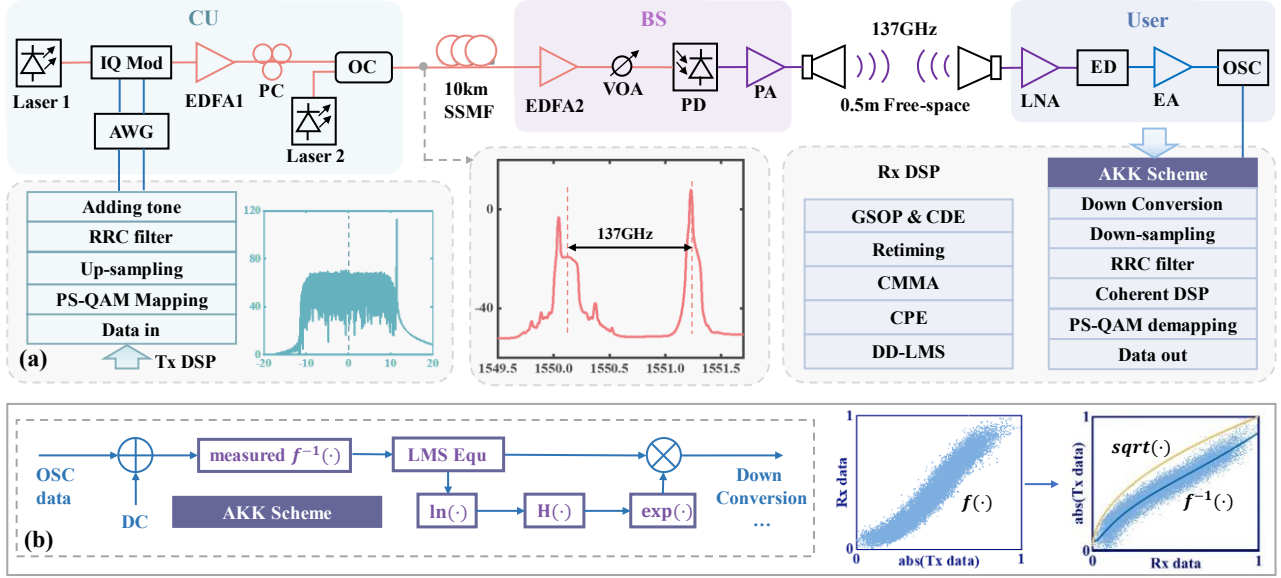


**Fig. 10.** (a) Experimental setup of PS simplified coherent photonics-aided fiber-THz integrated system with (b) AKK scheme.

193.3985 GHz using an IQ modulator (IQ Mod). This reduces the use of a laser in hardware meanwhile avoiding frequency offset at the receiver side caused by the different lasers and the computational complexity of correcting frequency offset in DSP block. The CSRR in the article was calculated from the signal power and the tone power in the digital domain. The optical signal was amplified by Erbium doped fiber amplifier 1 (EDFA1) and then coupled with the local oscillator light using a 1:1 optocoupler (OC) after through a polarization controller (PC). The signal spectrum after merging is plotted in Fig. 10. The frequency difference between the two beams of light was 137 GHz. Then, the signal passed through 10-km SSMF and was amplified by EDFA2 to compensate for link power loss, and the ROP-entering PD could be adjusted through a variable optical attenuator (VOA). Optoelectronic conversion occurred at the PIN-PD with a 3-dB bandwidth of 145 GHz, generating a THz signal with a center frequency of 137 GHz and a tone. The THz signal power was amplified and radiated into free space by the horn antenna. The operating frequency range of the power amplifier (PA) was 110-150 GHz, with a gain of 18 dB and a maximum input power of -3 dBm. The THz signal was received by another horn antenna after being transmitted about 0.5 meters in free space. The gain of these horn antennas was 25 dB.

The received THz signal was first amplified by a low noise amplifier (LNA) with an 18-dB gain, and then down-converted to intermediate frequency (IF) through an envelope detector (ED). After passing through the electric amplifier (EA), the IF signal was sampled and quantized by 80GSa digital storage oscilloscope (OSC), and converted to the digital domain for offline DSP. The operating frequency of LNA and ED was 110-170 GHz. The EA provided an amplification gain of approximately 23 dB for signals below 55 GHz.

The offline DSP at the receiving end sequentially included: conventional KK or AKK scheme to mitigate SSBI, or without KK for comparing performance, down conversion for converting signals from IF to baseband, down-sampling, matched filtering, classic coherent DSP algorithm, demapping

and then calculating EVM or normalized generalized mutual information (NGMI) to describe the performance of the communication system. The up-sampling rate used in all KK cases is 8. In the classic coherent DSP algorithm, as the first step, the Gram-Schmidt orthogonal projection (GSOP) was utilized to correct the I/Q imbalance, followed by clock recovery based on the fast square-timing-recovery algorithm. The signal was recovered by equalization based on the constant modulus algorithm (CMA). Following the carrier phase estimation (CPE), a decision-directed least mean square (DD-LMS) algorithm was employed to further enhance system performance. The AKK scheme is shown in Fig. 10(b), where the system AM-AM curves in the experiment were obtained through 16QAM signal with 1GHz bandwidth transmission under corresponding nonlinearity conditions.

The experiment used QPSK/16QAM/PS-64QAM modulation formats and conducted performance tests under different driving voltages, CSRR, ROP, and bandwidth. It should be noted that in the experiment, ED is a power detector, which satisfies the square-law detection. Furthermore, as indicated by subsequent results, when other nonlinearities in the system are negligible, the AM-AM curve of the system is approximately equal to the response curve of ED, which basically follows the shape of a square root. Derived from Eq. 4 and Eq. 6, as also as shown in Fig. 6 (a) & (d), the square law detection of ED makes GKK and traditional KK equivalent. Therefore, it can be inferred that there is no difference in performance between GKK and traditional KK in our experimental system. Therefore, it can be inferred that the performance of GKK is similar to that of KK. In the following analysis, we conduct the performance comparison between AKK, w.o. KK and KK/GKK (squared).

### B. Results and Analysis

Fig. 11 shows the EVM curves of QPSK with a bandwidth of 12.5 GHz as a function of  $V_{pp}$ , CSRR and ROP, respectively. As  $V_{pp}$  increases, the EVM of QPSK signal firstly decreases and then increases, corresponding to performance first increasing and



> REPLACE THIS LINE WITH YOUR MANUSCRIPT ID NUMBER (DOUBLE-CLICK HERE TO EDIT) <

then decreasing. The reason for this trend is that the increase in  $V_{pp}$  leads to an increase in signal power, resulting in an improvement in SNR and performance. On the other hand, the continuously increasing  $V_{pp}$  also leads to an increase in system nonlinearity. Under the combined effect of SNR and nonlinearity, the optimal performance point is at  $V_{pp}$  500 mV. In terms of performance of AKK, it is significantly better than w.o. KK and KK/GKK (squared) at each  $V_{pp}$ . At higher  $V_{pp}$  with stronger nonlinearity, AKK has more obvious superiority. The illustration in Fig. 11(a) shows the received constellations of w.o. KK and AKK at  $V_{pp}$  500 mV. It can be seen that AKK reduces the influence of nonlinearity on symbols, and the contour of each constellation point is closer to a regular circle. The results of (b) and (c) were all measured at a  $V_{pp}$  of 500 mV. Fig. 11(b) shows the variation of EVM with CSPR. As low CSPR condition does not meet the minimum phase rule and high CSPR has poor SNR, AKK achieves the best performance when CSPR is 9 dB. The

illustration in Fig. 11(b) shows the fitted AM-AM curve of the system at 500-mV  $V_{pp}$  and 6-dBm ROP. It can be seen that the nonlinearity at this point is significant, forming an emphatic gap with the ideal square root curve. At this point, using a response curve that is closer to the real experimental system and applying an LMS equalizer to eliminate part of ISI are the reasons that AKK performs better. Fig. 11(c) displays the variation of EVM with ROP. In an ideal situation, the larger the ROP, the higher the THz signal power generated by photoelectric conversion. Under other unchanged conditions, the system transmission performance is better. However, PD exhibits saturated power and nonlinear effects, causing performance to gradually decline when ROP is too high. The higher the ROP, the stronger the nonlinearity of the system, so AKK also shows more improvement at higher ROP under both back-to-back (B2B) and 10-km SSMF transmission. The illustration in Fig. 10(c) shows the AM-AM curve of the system when the ROP is 3 dBm. Obviously, it is closer to the ideal square root curve than when the ROP is 6 dBm.

16QAM signal was transmitted, and the results are shown in Fig. 12. Similar to the results of QPSK, AKK processing still maintains significant superiority when  $V_{pp}$ , CSPR and ROP changing. The illustration in Fig. 12(a) shows the AM-AM curves with  $V_{pp}$  of 300 mV and 700 mV, corresponding to the presence of weak and strong nonlinearity in the system, respectively. The illustrations in Fig. 12(b) show the received constellations without KK and using AKK scheme when CSPR is 7 dB, respectively. It can be seen that constellations after using AKK become clearer, especially for outer constellations that are severely affected by nonlinearity. At the NGMI threshold of 0.8574, compared to w.o. KK, AKK exhibits a larger driving voltage range, with a minimum CSPR reduction of about 2-dB and 1-dB sensitivity improvement. These gains are beneficial for reliable transmission of the system over a larger dynamic range and lower costs. In terms of baud rate, the AKK scheme supports 19-GHz 16QAM signal transmission, with a line rate of 76 Gbps and a net rate of 61.54 Gbps. The illustration in Fig. 12(d) shows the AKK received constellations with bandwidths of 7.5 GHz and 19 GHz. Our experimental system performance is mainly limited by the bandwidth of PD and PA. Therefore, strong ISI and low SNR make the constellations blurry and scattered at large bandwidths.

To further study the proposed scheme in flexible coded modulation scheme, such as PS, we have conducted the following tests. PS is one of the solutions to achieve flexible rate. When the NGMI performance of the system is significantly higher than the current threshold (0.8574 here), it may be appropriate to regard PS to increase the source entropy, so that the NGMI of the PS signal is close to the threshold, in exchange for a higher rate. On the contrary, when the system is operating in a state that does not meet performance requirements, PS could be used to suitably reduce the source entropy at the cost of reducing tolerable rates to meet the threshold. Based on the above results, we experimented with PS-64QAM, striving to utilize all resources at various ROPs and baud rates to achieve the highest possible transmission rate. On the basis of applying PS technology to adjust source entropy, in order to highlight the advantages of AKK scheme, the transmission entropy is adjusted by changing the Maxwell-Boltzmann distribution scaling factor

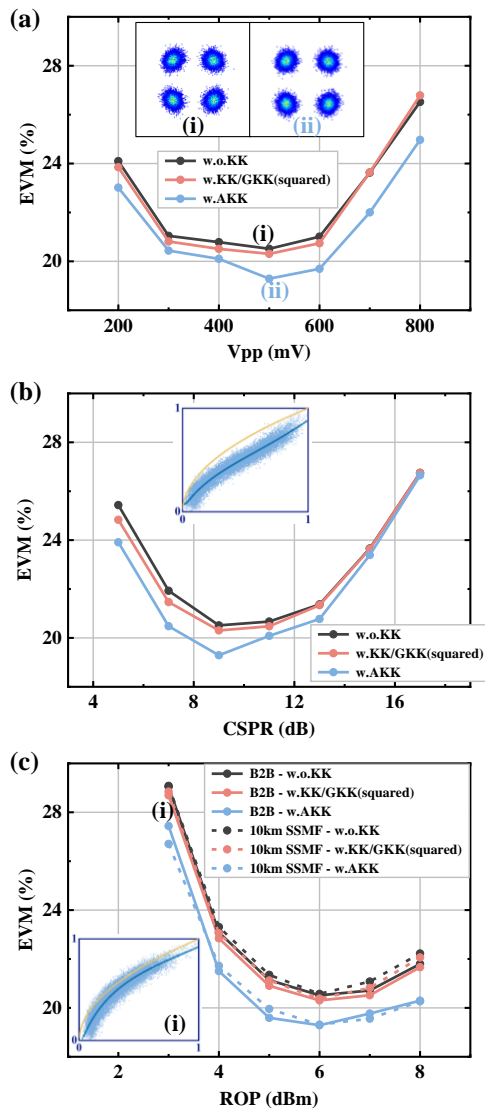


**Fig. 11.** Parameters affecting the performance of AKK scheme: (a) EVM as a function of  $V_{pp}$  for 12.5-GbD QPSK signal, (b) EVM as a function of CSPR for 12.5-GbD QPSK signal and (c) EVM as a function of ROP.

> REPLACE THIS LINE WITH YOUR MANUSCRIPT ID NUMBER (DOUBLE-CLICK HERE TO EDIT) <

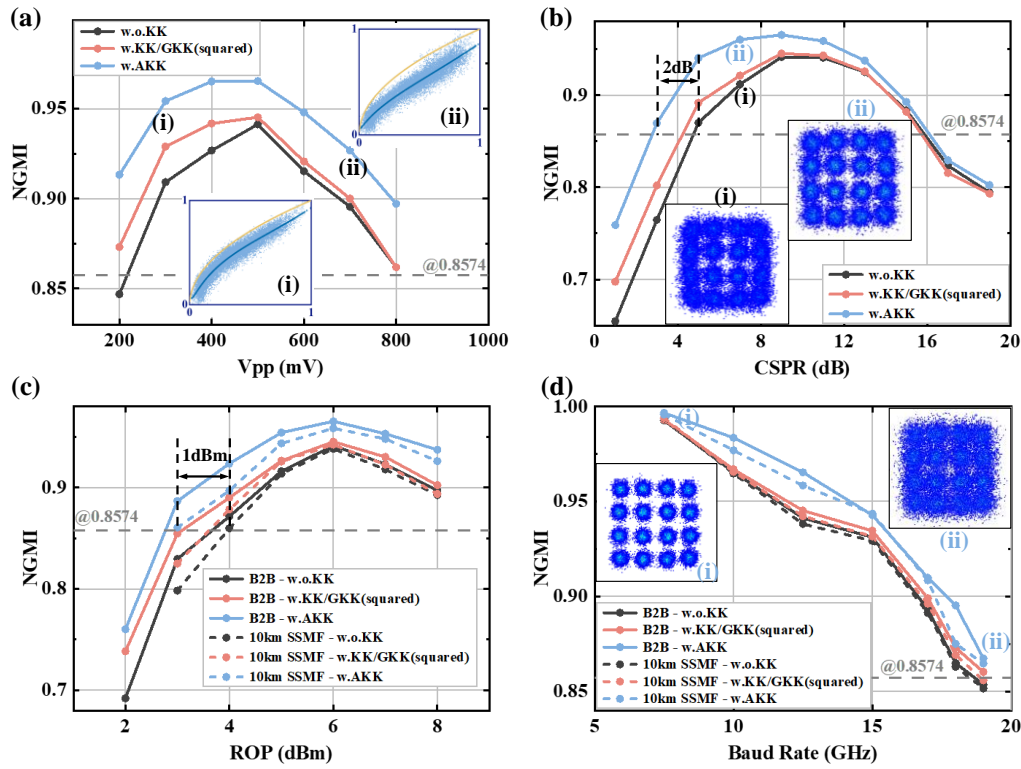


**Fig. 12.** Parameters affecting the performance of AKK scheme: NGMI as a function of (a)  $V_{pp}$ , (b) CSRR, (c) ROP for 12.5-GBd 16QAM signal and (d) NGMI as a function of Baud Rate for 16QAM signal.

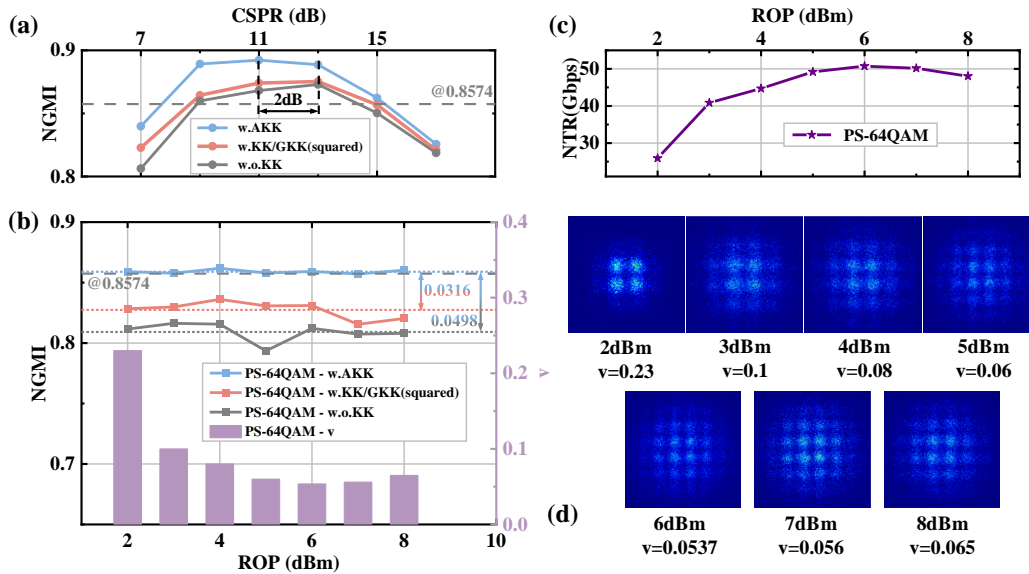


**Fig. 13.** (a) NGMI as a function of CSRR for 12.5-GBd PS-64QAM signal with 0.07  $v$ , (b) NGMI &  $v$  as functions of ROP for PS-64QAM signal when using AKK could precisely meet the NGMI threshold, (c) the NTR and (d) the received constellation using AKK corresponding to (b).

$v$  [29] under different conditions was adjusted to ensure that the NGMI after doing AKK exactly accesses the NGMI threshold, and then compared performance under the same  $v$  value.

The optimal CSRR of PS-64QAM firstly was searched for and found that it became 11 dB, which is different from QPSK and 16QAM, as shown in Fig. 13(a). The PS-64QAM signal with  $v=0.07$  was transmitted, with a bandwidth of 12.5 GHz and a ROP of 6dBm. In fact, the performances of AKK when CSRR is

9, 11 and 13 dB are very close, while the performance of w.o. KK and GKK (squared) at the optimal 13-dB CSRR is very conspicuous. The AKK processing shows a 2-dB reduction of the optimum CSRR compared to heterodyne reception w.o. KK processing and GKK (squared), and there are larger CSRR adjustment range that meet the threshold. AKK's advantages of expanding dynamic range and saving resources are ulteriorly demonstrated. The following results were tested at CSRR 11 dB.

> REPLACE THIS LINE WITH YOUR MANUSCRIPT ID NUMBER (DOUBLE-CLICK HERE TO EDIT) <

16QAM signal with 12.5 GBd could transmit within the ROP 3-8 dBm range, therefore the transmit source entropy of AKK PS-64QAM was adjusted within the range of ROP 2-8 dBm to meet the NGMI threshold. Fig. 13(b) shows the NGMI values that meet the threshold for AKK processing and those without KK processing at each ROP, with corresponding  $v$  values displayed in a bar chart. AKK processing results in an average NGMI gain of 0.0498 compared to w.o.KK and 0.0316 compared to GKK. Fig. 13(c) illustrates the net transmission rate (NTR) achieved by PS-64QAM at different ROPs. AKK PS-64QAM not only enables reliable system operation at ROP 2 dBm but also increases transmit entropy to enhance system transmission rates when ROP is high and SNR has redundancy. Fig. 13(d) presents the received constellations for AKK PS-64QAM corresponding to different ROPs.

Similarly, transmission experiments using PS-64QAM were conducted with different bandwidths. The maximum NTRs achieved of both AKK processing 16QAM and PS-64QAM at each bandwidth are shown in Fig. 14(a). Below 18-GHz bandwidth, the rate improvement brought by PS is evident. However, at 18 GHz and 19 GHz, the NTRs achieved of PS-64QAM signal are slightly lower than those of 16QAM signal. This might be due to the fact that the performance of 16QAM is already close to the threshold, and the redundancy in capacity is insufficient to support the cost and overhead required for increasing the modulation order and using PS, including increases in PAPR and higher SNR requirements. Fig. 14(b) specifically compares the NGMI values for PS-64QAM with and without AKK processing at each bandwidth. Fig. 14(c) displays the AKK PS-64QAM constellations for bandwidths other than 12.5 GHz. At a 19-GHz bandwidth, transmission of PS-64QAM signal successfully achieved the system peak line rate exceeding 80 Gbps.

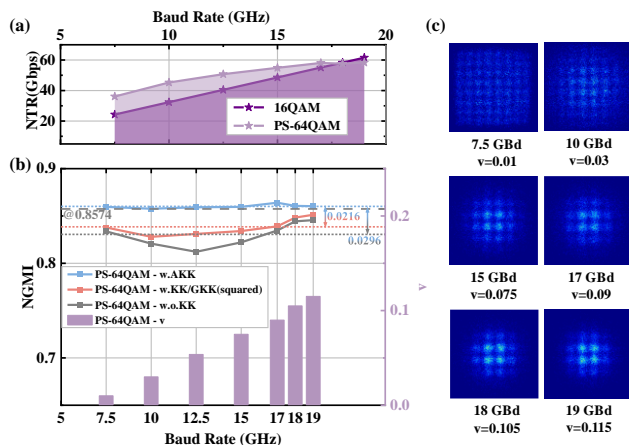


**Fig. 14.** (a) NTR as a function of Baud Rate, (b) NGMI &  $v$  as functions of Baud Rate for PS-64QAM signal when using AKK could precisely meet the NGMI threshold, (c) the received constellation using AKK corresponding to (b).

## V. CONCLUSION

A simplified coherent photonics-aided D-band fiber-THz integrated system with AKK scheme based on PS-QAM modulations was demonstrated. The strength of AKK scheme

in resistance to nonlinearity and ISI compared to GKK was verified by both simulations and experiments. Experimental results indicated that AKK can widen the dynamic range of driving voltage, with a minimum CSCR reduction of about 2dB and 1dB sensitivity improvement compared to w.o. KK. Generating a single sideband signal in digital domain reduces the use of a laser in hardware meanwhile avoiding frequency offset at the receiver side and the computational complexity of correcting frequency offset in DSP. The proposed scheme works well in the flexible PS-based fiber-THz integrated communication systems. The NGMI gain also exists when using PS technology, and a line rate of over 80 Gbps and a net rate of over 60 Gbps are realized through 10-km SSMF and 0.5-m wireless distance at 137-GHz fiber-THz integrated communication system.

## ACKNOWLEDGMENT

This work was supported in part by the National Key Research and Development Program of China under Grant 2022YFB2903600, in part by the National Natural Science Foundation of China under Grants 62235005, 62171137, 61925104, and 62071444, in part by the Natural Science Foundation of Shanghai under Grant 21ZR1408700, and in part by the Major Key Project PCL.

## REFERENCES

- [1] W. Saad, M. Bennis and M. Chen, "A vision of 6G wireless systems: Applications trends technologies and open research problems," *IEEE Netw.*, vol. 34, no. 3, pp. 134-142, May/Jun. 2020, doi: 10.1109/MNET.001.1900287.
- [2] M. Z. Chowdhury, M. Shahjalal, S. Ahmed and Y. M. Jang, "6G wireless communication systems: Applications requirements technologies challenges and research directions," *IEEE Open J. Commun. Soc.*, vol. 1, pp. 957-975, 2020, doi: 10.1109/OJCOMS.2020.3010270.
- [3] H. Elayan, O. Amin, B. Shihada, R. M. Shubair and M. -S. Alouini, "Terahertz band: The last piece of RF spectrum puzzle for communication systems," *IEEE Open J. Commun. Soc.*, vol. 1, pp. 1-32, 2020, doi: 10.1109/OJCOMS.2019.2953633.
- [4] I. F. Akyildiz, A. Kak and S. Nie, "6G and beyond: The future of wireless communications systems," *IEEE Access*, vol. 8, pp. 133995-134030, 2020, doi: 10.1109/ACCESS.2020.3010896.
- [5] L. Zhang, X. Pang, S. Jia, S. Wang and X. Yu, "Beyond 100 Gb/s optoelectronic terahertz communications: Key technologies and directions," *IEEE Commun. Mag.*, vol. 58, no. 11, pp. 34-40, Nov. 2020, doi: 10.1109/MCOM.001.2000254.
- [6] T. Nagatsuma, G. Ducournau and C. C. Renaud, "Advances in terahertz communications accelerated by photonics," *Nature Photon.*, vol. 10, no. 6, pp. 371, 2016, doi: 10.1038/NPHOTON.2016.65.
- [7] T. Nagatsuma et al., "Millimeter-wave and terahertz-wave applications enabled by photonics," *IEEE J. Quantum Electron.*, vol. 52, no. 1, pp. 1-12, Jan. 2016, doi: 10.1109/JQE.2015.2506992.
- [8] K. Li and J. Yu, "Photonics-aided terahertz-wave wireless communication," *J. Lightw. Technol.*, vol. 40, no. 13, pp. 4186-4195, Jul. 2022, doi: 10.1109/JLT.2022.3161878.
- [9] C. Wang, J. Yu, X. Li, P. Gou, and W. Zhou, "Fiber-THz-fiber link for THz signal transmission," *IEEE Photon. J.*, vol. 10, no. 2, Apr. 2018, Art. no. 7200706, doi: 10.1109/JPHOT.2018.2809433.
- [10] X. Li, J. Yu, J. Zhang, Z. Dong, F. Li, and N. Chi, "A 400 G optical wireless integration delivery system," *Opt. Express*, vol. 21, no. 16, pp. 18812-18819, 2013.
- [11] C. Castro, R. Elschner, T. Merkle, C. Schubert, and R. Freund, "Experimental demonstrations of high-capacity THz-wireless transmission system for beyond 5G," *IEEE Commun. Mag.*, vol. 58, no. 11, pp. 41-47, Nov. 2020, doi: 10.1109/MCOM.001.2000306.
- [12] M. S. Erkinç et al., "Comparison of low complexity coherent receivers for UDWM-PONs ( $\lambda$ -to-the-user)," *J. Lightw. Technol.*, vol. 36, no. 16, pp. 3453-3464, Aug. 2018, doi: 10.1109/JLT.2018.2835376.

> REPLACE THIS LINE WITH YOUR MANUSCRIPT ID NUMBER (DOUBLE-CLICK HERE TO EDIT) <

- [13] A. Hraghi, G. Rizzelli, A. Pagano, V. Ferrero, and R. Gaudino, "Analysis and experiments on C band 200G coherent PON based on alamouti polarization-insensitive receivers," *Opt. Exp.*, vol. 30, no. 26, pp. 46782–46797, 2022.
- [14] M. S. Faruk, X. Li, and S. J. Savory, "Experimental demonstration of 100/200-Gb/s/λ PON downstream transmission using simplified coherent receivers," in *Optical Fiber Communication Conference (OFC) 2022*, San Diego, California, 2022, p. Th3E.5.
- [15] A. Mecozzi et al., "Kramers–Kronig coherent receiver," *Optica*, vol. 3, no. 11, pp. 1220–1227, Jun. 2016, doi: 10.1364/OPTICA.3.001220.
- [16] T. Harter et al., "Generalized Kramers–Kronig receiver for coherent terahertz communications," *Nature Photon.*, vol. 14, no. 10, pp. 601–606, 2020, doi: 10.1038/s41566-020-0675-0.
- [17] Y. Cai et al., "Spectrally efficient PDM-Twin-SSB direct-detection THz system without active polarization control," *IEEE Photon. Technol. Lett.*, vol. 35, no. 15, pp. 838–841, Aug. 2023, doi: 10.1109/LPT.2023.3275921.
- [18] P. Luo et al., "Simplified coherent photonics-aided W-band fiber-mmW integrated system with adaptive Kramers-Kronig scheme," in *European Conference on Optical Communication (ECOC) 2023*, Glasgow, Scotland, 2023, pp. 1–4.
- [19] S. Wang et al., "26.8-m THz wireless transmission of probabilistic shaping 16-QAM-OFDM signals," *APL Photon.*, vol. 5, no. 5, 2020, Art. no. 056105, doi: 10.1063/5.0003998.
- [20] J. Ding et al., "Demonstration of 32-Gbit/s Terahertz-Wave signal transmission over 400-m wireless distance," in *European Conference on Optical Communication (ECOC) 2022*, Basel, Switzerland, 2022, pp. 1–4.
- [21] W. Li et al., "Probabilistic shaping-assisted bit-energy efficient THz photonic wireless transmission," in *Proc. 45th Eur. Conf. Opt. Commun.*, 2019, Art. no. Th2C.1, doi: 10.1049/cp.2019.0997.
- [22] I. -H. Baek et al., "Time Adaptive Probabilistic Shaping for Combined Optical/THz Links," in *Photonic Networks; 23th ITG-Symposium*, Berlin, Germany, 2022, pp. 1–8.
- [23] F. R. Kschischang and S. Pasupathy, "Optimal nonuniform signaling for Gaussian channels," *IEEE Trans. Inf. Theory*, vol. 39, no. 3, pp. 913–929, May 1993, doi: 10.1109/18.256499.
- [24] B. J. C. Schmidt, A. J. Lowery and L. B. Du, "Low sample rate transmitter for direct-detection optical OFDM," 2009 Conference on Optical Fiber Communication, San Diego, CA, USA, 2009, pp. 1–3, doi: 10.1364/OFC.2009.OWM4.
- [25] P. Wei-Ren, W. Xiaoxia, V. R. Arbab, B. Shamee, L. C. Christen, Y. Jeng-Yuan, F. Kai-Ming, A. E. Willner, and C. Sien, "Experimental demonstration of a coherently modulated and directly detected optical OFDM system using an RF-Tone insertion," presented at Optical Fiber communication/National Fiber Optic Engineers Conference, 2008. OFC/NFOEC 2008, San Diego, CA, paper OMU2, 2008.
- [26] J. Jia, J. Zhang and N. Chi, "Constellation shaping optimization for nonlinearity mitigation in CAP UVLC system," *Sci. China Inf. Sci.*, vol. 66, no. 9, pp. 192–305, Sep. 2023, doi: 10.1007/s11432-022-3643-y.
- [27] R. Schmogrow et al., "Error Vector Magnitude as a Performance Measure for Advanced Modulation Formats," in *IEEE Photonics Technology Letters*, vol. 24, no. 1, pp. 61–63, Jan.1, 2012, doi: 10.1109/LPT.2011.2172405.
- [28] A. J. Lowery, T. Wang and B. Corcoran, "Enhanced Kramers-Kronig Single-Sideband Receivers," in *Journal of Lightwave Technology*, vol. 38, no. 12, pp. 3229–3237, 15 June15, 2020, doi: 10.1109/JLT.2020.2985423.
- [29] Z. Qu and I. B. Djordjevic, "On the Probabilistic Shaping and Geometric Shaping in Optical Communication Systems," in *IEEE Access*, vol. 7, pp. 21454–21464, 2019, doi: 10.1109/ACCESS.2019.2897381.